



19 **Abstract**

20 Understanding sequestration of organic carbon (C) in agroecosystems is of primary importance  
21 for greenhouse gas (GHG) accounting in managed ecosystems, reducing the environmental footprint  
22 of land use, and inform crediting programs. However, a broader application of precise C accounting  
23 is currently constrained by a limited number of direct flux measurements. Aside well-studied  
24 ecosystems via the eddy-covariance technique (EC), many still bear significant uncertainty. In this  
25 study, we propose and evaluate a method for estimating accumulated C stocks in agricultural sites,  
26 by assessing the plant aboveground carbon (AGC) throughout the growing season using mobile  
27 platforms and machine learning (ML) regression methods. Then, we benchmark these estimates  
28 with  $CO_2$  fluxes derived from the EC method from the ICOS DK-Vng site in Denmark. We  
29 utilized a light detection and ranging (LiDAR) sensor onboard an unstaffed aerial vehicle (UAV)  
30 to derive the structural characteristics of crops, and we conducted in parallel destructive field-  
31 based measurements of AGC. Then, we designed a ML pipeline to provide estimates of AGC as  
32 a supervised regression problem, using the LiDAR-derived point cloud data to extract predictive  
33 features and the AGC labels as ground-truth target values. The best performing ML model attained  
34 predictions of  $R^2 = 0.71$  and  $R^2 = 0.93$  at spatial resolutions of  $1\ m^2$  and  $2\ m^2$ , respectively. The  
35 C content in the aboveground plant components was assessed via laboratory analysis ( $46.6 \pm$   
36  $0.3\%$  of C-to-biomass in barley and  $47.7 \pm 0.3\%$  in wheat), while the belowground components  
37 (root allocation and rhizodeposition) were estimated based on a phenology-dependent allometric  
38 ratio. The cumulative value of C uptake along the growing season (i.e. NPP) was compared with  
39 the difference of C predictions between every two UAV-LiDAR survey dates, finding an optimal  
40 disagreement between methods below  $\pm 10\%$  in two different cereal crops. Various experimental  
41 set-ups are evaluated as well as the sources of uncertainty resulting from the sampling design.

42

---

43 **This PREPRINT manuscript is currently being considered for formal peer-reviewed**  
44 **publication. Please note that, this is the submitted version of the study, and has yet**  
45 **to be formally accepted. Subsequent versions of this manuscript may present slight**  
46 **differences in content. If accepted, the final version of this manuscript will be**  
47 **updated with the accepted manuscript. This preprint will also be linked to the**  
48 **formal publication via its Digital Object Identifier (DOI). Please, feel free to contact**  
49 **any of the authors; we welcome feedback.**

---

50



51 **= Introduction =**

52 The agricultural sector is the world’s second-largest greenhouse gas (GHG) emitter, after the  
 53 energy sector, accounting for a quarter of total global anthropogenic GHG emissions [1]. While  
 54 agriculture is a driver of climate change, the observed climate alterations have in turn challenged  
 55 the global crop productivity in the last decades [2, 3]. In the absence of technological adaptations  
 56 and dedicated mitigation measures [4], the environmental effects of agriculture could increase by  
 57 50–90 % [5], and the global crop productivity might be reduced a 17 % by 2050 [6]. However, in  
 58 most countries, the accounting of emissions for land-use and agriculture relies on simple upscaling  
 59 of standardized values, with little to no data-driven validation procedures. To date, the adoption  
 60 of climate-resilient and low-emission practices in agriculture has not yet reached the recommended  
 61 levels [5]. This is hindering accurate GHG accounting as well as attaining environmental and  
 62 economically efficient solutions.

63 Monitoring carbon (C) sequestration and CO<sub>2</sub> emissions from croplands is a prerequisite for  
 64 the effective design of sustainable agricultural management schemes. In a changing global climate,  
 65 different regions undergo contrasting extreme weather events such as drought, heavy precipitation,  
 66 shifts in timing and length of growing seasons, or heat stress [7]. This highlights the necessity to  
 67 quantify the C sequestration capacity with techniques tailored to specific ecosystems’ conditions.  
 68 In this context, precision agriculture (PA) is regarded as a promising set of methods for sustainable  
 69 intensification, in order to close yield gaps while reducing GHG emissions [8, 9, 10]. PA targets  
 70 the reduction of agriculture’s impact on the environment, while optimizing crop yield [11] with  
 71 data-driven methods.

72 The standard framework to account for the transit of atmospheric CO<sub>2</sub> is the net ecosystem  
 73 exchange (NEE) [12], i.e. the net CO<sub>2</sub> flux at the atmosphere-biosphere interface (Figure 1). NEE  
 74 is calculated as the difference between CO<sub>2</sub> uptake (i.e. gross primary productivity, GPP) and  
 75 release of CO<sub>2</sub> via respiratory losses ( $R_{eco}$ ) [12]. Another commonly used magnitude in ecosystem  
 76 budgeting is the net primary productivity (NPP) that, compared to NEE, does not explicitly  
 77 include soil-derived fluxes and heterotrophic respiration, therefore reflecting the photosynthetic  
 78 productivity of vegetation alone [13]. Thus, NPP is the most direct surrogate measure for plant  
 79 growth provided by the flux-based eddy covariance framework.

80 At the ecosystem scale, C budgets are usually reported as a range of confidence for C estimates,  
 81 rather than specific values [14]. This is due to the fact that ecosystem-level estimates are bound  
 82 to co-occurring complex phenomena, so that it is necessary to count on certain assumptions (e.g.  
 83 negligible levels of lateral carbon fluxes and heterotrophic respiration, atmospheric turbulence  
 84 conditions reached, etc.) which affects the estimates’ accuracy. In fact, studies focused on different  
 85 regions have reported large inter-annual variability in C fluxes from croplands, which act either as  
 86 net sinks [15], net sources [16, 17], or as relatively C neutral [18].

87 In order to assess the consistency of the net ecosystem carbon balance (NECB), established  
 88 approaches involve comparing a measured quantity (e.g. NEE) obtained at the same temporal  
 89 and spatial scale using independent methods [19, 20, 21, 22, 23]. This can be done via either: (i)  
 90 micrometeorological methods to assess the ecosystem-atmosphere fluxes; (ii) inventories of stock  
 91 changes in the biomass and soil; or (iii) bottom-up modelling of ecophysiological processes from  
 92 flux chamber measurements. Such consistency assessments require that all NECB components are  
 93 estimated during the same time intervals [24].

94 In practice, the components of the NECB are directly measured by the eddy-covariance (EC)  
95 technique or derived from such measurements [25], which is to date the state-of-the-art to obtain  
96 ecosystem-level flux estimates. However, there are limitations associated with the EC method,  
97 namely, (i) being bound to local measurements with costly instrumentation fixed to the ground,  
98 and (ii) requiring specific atmospheric conditions. This entails the need to assume that areas  
99 monitored by the EC method are representative of broadly defined ecosystem types. However,  
100 observational gaps exist [26] and single ecosystem types may not be sufficiently account for the  
101 effects of diverse environmental conditions and management practices. Hence, it is needed to  
102 advance methods to improve the flexibility of C estimates, where approaches based on mobile  
103 platforms have proven useful [27, 28, 29, 26].

104 The main interest in advancing unstaffed aerial vehicle (UAV)-based methods lies in profiting  
105 from the flexibility and scalability that mobile platforms provide, thereby gaining independence  
106 from restrictions associated to the use of fixed instrumentation. In the last decade, UAV methods  
107 employed to monitor fluxes and crop status have provided significant advances. Hoffmann et al.  
108 (2016) [27] investigated the potential of UAV imagery-based estimates to provide crop water stress  
109 maps in barley fields. Recently, Hollenbeck and Chen (2021) [28] presented a method using multiple  
110 UAVs for assessing continuous flows inside emission plumes. Also, Hollenbeck et al. (2022) [29]  
111 proposed a method for quantifying ecosystem-based fluxes, by flying upwind and downwind the  
112 emission source point, and evaluating gradients. The integration of UAV-based data and ecosystem  
113 modelling has also been explored: Wang et al. (2020) [26] introduced a method for estimating  
114 interpolated land surface fluxes derived from a combination of UAV-based imagery and a dynamic  
115 soil-vegetation-atmosphere model, finding that the UAV-based method proved useful in calibrating  
116 soil and vegetation parameters, achieving C flux estimates within 13-15% of agreement with the  
117 EC measurements.

118 Furthermore, UAV-based remote sensing is being increasingly applied to assess aboveground  
119 biomass (AGB) and C stocks due to the ability of mobile sensors to capture the spatial distribution  
120 of land surface variables at high spatial resolution and flexible revisit times [30]. It has been proven  
121 useful to complement EC measurements to estimate fluxes where data monitoring is limited [26].  
122 To date, the majority of studies use UAV-photogrammetry (e.g. structure-from-motion techniques)  
123 to calculate AGB as a function of plant height metrics (e.g. maize [31, 32, 33], corn [34], rice [35],  
124 barley [36, 37] cotton [38], or winter wheat [39, 40]). Yet another line of research aims to assess  
125 AGB as a function of vegetation indices using spectrally resolved sensors in different cash and food  
126 crops (e.g. spring wheat [41], winter wheat [42, 43, 44], corn and soybean [45], and rice [46]).

127 More recently, the advent of mobile light detection and ranging sensors (LiDAR) has not only  
128 upgraded the spatial resolution of data sets, but also included the vertical component, creating truly  
129 volumetric representations (i.e. point clouds). This has allowed to enhance crop phenotyping [47]  
130 and map AGB in croplands at a sub-meter resolution [30] by leveraging the structural informa-  
131 tion of vegetation from 3D point clouds. UAV-LiDAR methods have provided a workaround to  
132 previous obstacles in UAV-based crop phenotyping, namely the spectral saturation in image-based  
133 vegetation indexes, especially during maturity of crops.

134 In this study, we explore the level of agreement between two independent methods: (i) UAV-  
135 LiDAR surveying to monitor the temporal development of plant C and (ii) flux-based EC measure-  
136 ments. These methods were employed to obtain simultaneous estimates of assimilated atmospheric  
137 C stocks in a crop field, which was subjected to a cereal crop rotation scheme over two consecutive

138 years. Specifically, we propose and evaluate a method to estimate *in situ* plant C at the plot scale  
 139 using UAV-LiDAR and machine learning (ML) regressions, and compare the results obtained with  
 140 the respective NPP during identical time intervals.

141 The motivation of this study is to leverage the capabilities of UAV-LiDAR sensors and a ML-  
 142 based approach in order to provide estimates of plant C stocks in croplands, thereby contributing  
 143 to advancing current techniques in ecosystem C budgeting from mobile platforms.

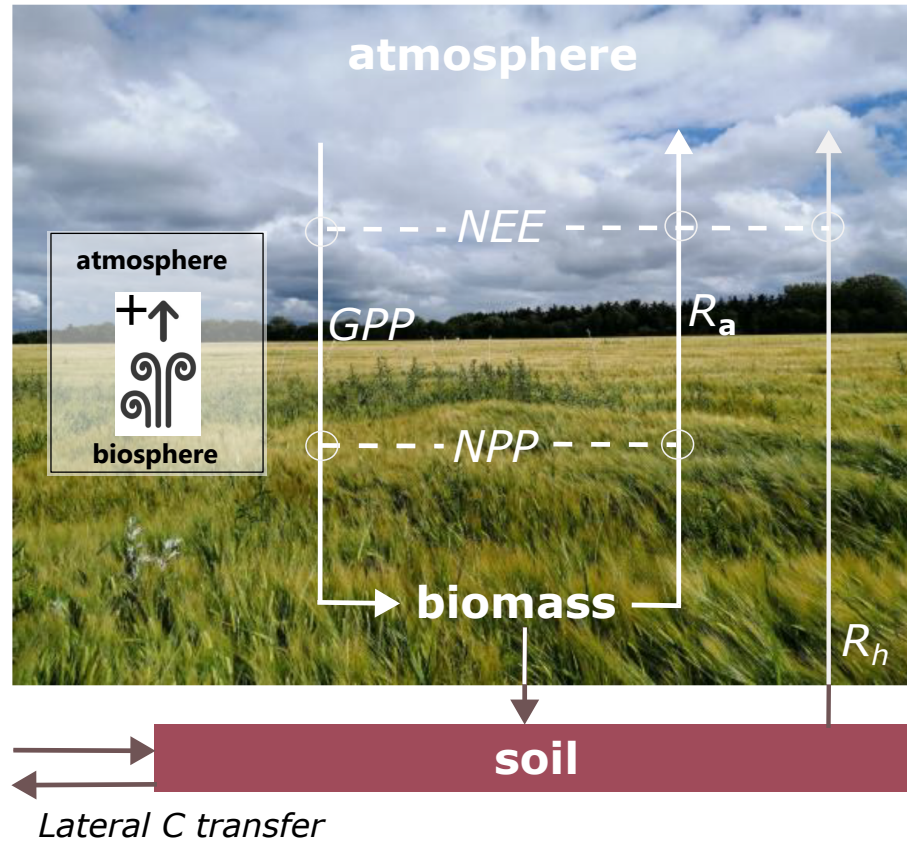


**Figure 1.** Components of the net ecosystem carbon balance (NECB). The inset on the left indicates the sign convention for fluxes calculation. NEE: net ecosystem exchange. GPP: gross primary productivity. NPP: net primary productivity. NEE: net ecosystem exchange.  $R_a$ : autotrophic respiration.  $R_h$ : heterotrophic soil respiration. Lateral carbon transfer refers to human intervention (e.g. harvest, fertilization).

144 = **Materials and Methods** =

145 **Study Area**

146 The study area (Figure 2) is a conventionally managed cropland site located around an Inte-  
 147 grated Carbon Observation System (ICOS) [48] class-1 ecosystem station at Voulund, (DK-Vng)  
 148 in Mid-Jutland, Denmark (56.037476N, 9.160709E). Located on the eastern part of the Skjern  
 149 River catchment, covering an area of ca. 13 ha. The field is a flat plain at an altitude of 64-68 m  
 150 above mean sea level, with smooth undulations and a slight slope to the northwest. The ploughing

151 layer (30 cm deep) sits on a sandy soil (>99%) with pebble inclusions of ca. 3-5 diameter. The  
 152 water-table depth lies at  $5.5 \pm 1$  m below ground. The region presents a humid temperate climate  
 153 characterized by a mean annual precipitation of 961.0 mm, mean annual temperature of 8.1 °C,  
 154 and usually overcast or scattered cloud cover (mean annual incoming short-wave radiation of 108  
 155  $W/m^2$ ). For an insightful description of both functional and topographic characteristics of the  
 156 Voulund agricultural site, the reader is referred to Jensen et al. (2016) [18]



**Figure 2.** Location of the study site (★) in Mid-Jutland (DK). The inset shows a top-down view of the field site and the surrounding area. Source: [www.icos-cp.eu](http://www.icos-cp.eu) and Google Earth Engine.

157 The crops investigated were spring barley (*Hordeum vulgare L.*) and winter wheat (*Triticum*  
 158 *aestivum L.*) during 2020 and 2021. The growing period of the barley crops lasted from the end of  
 159 04/2020 (seedling emergence) to the end of 08/2020 (harvest), following a similar cycle in the 2021  
 160 season. In 2021, the growing period of winter wheat extended from 01/2021 (seedling emergence)  
 161 until the end of 08/2021 (harvest). The conventional agricultural practice at the site included  
 162 the application of fertilizers in the form of pig slurry, according to ministerial regulations [49],  
 163 pesticides and fungicides along the growing season, as well as sufficient irrigation to prevent water  
 164 stress [18]. This corresponds to a maximum amount of fertilizer of 159 (N) and 21 (P) kg/ha and  
 165 202 (N) and 19 (P) kg/ha for spring barley and winter wheat, respectively.

### 166 UAV-LiDAR Survey and Point Cloud Data

167 We used a UAV-borne LiDAR system mounted to a DJI Matrice 600 Pro payload at a 90° pitch  
 168 angle, and same heading and roll as the UAV platform. The system included a discrete infrared  
 169 LiDAR scanner (M8 sensor, Quanenergy Systems, Inc. Sunyvale, CA, USA) and the corresponding  
 170 industry standard inertial and navigation systems. In addition, we used a ground based differential  
 171 Global Positioning System (dGPS, Trimble R8) during the UAV-LiDAR survey, set up in post-  
 172 positioning kinematic (PPK) mode, which logged real-time satellite coverage (cf. Ravenga et al.  
 173 2022 [30] for details on the airborne and ground system). The coupling of the satellite coverage data  
 174 with the UAV-based laser and navigation data produced allowed the generation of georeferenced

175 point cloud data (PCD) scenes, following Davidson et al. (2019) [50]. We visualized the PCD  
 176 scenes of barley and wheat crops at maturity stage in Figure 3 (a and b, respectively). It can  
 177 be noted how the PCD scenes reflect a higher porosity in the crops of 2021, than in 2020. This  
 178 corresponds to a more sparse canopy structure in the second year than in the first (Figure 5, a.2  
 179 and b.2).

180 UAV-LiDAR data were acquired according to the planned UAV-LiDAR survey at a height  
 181 of 40 m above ground level. Following a regular auto-pilot flight grid, we ensured a 20% overlap  
 182 between individual LiDAR scans of ca. 50 m width and 250 pp/m<sup>2</sup> (cf. Revenga et al. 2022 [30]  
 183 for additional details on applied flight parameters). The surveys were conducted during May-July  
 184 2020, and during April-July 2021, coinciding with the two growing seasons.

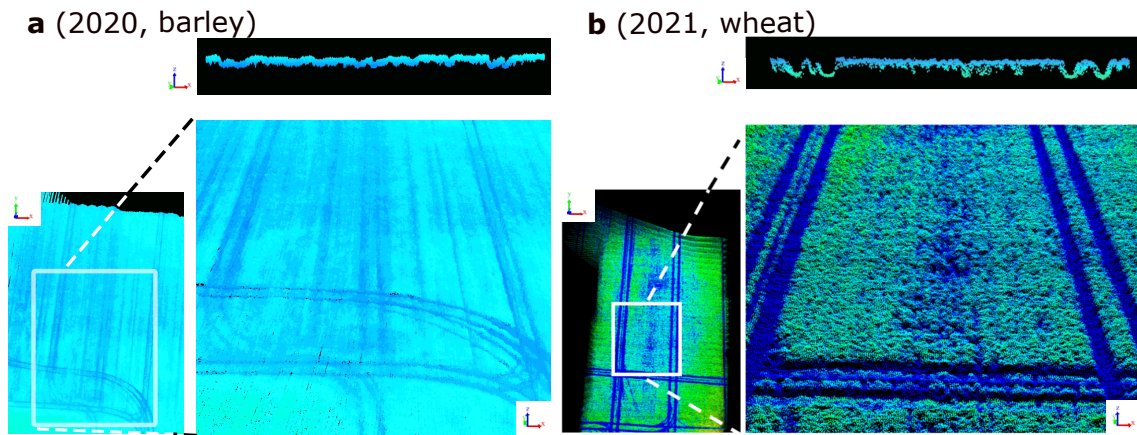


**Figure 3.** Point cloud data (PCD) scenes. The crops are portrayed at maturity stage. **a:** barley field, during 2020. **b:** wheat field, during 2021. The PCD scenes are colored by elevation. In both **a** and **b**, the upper panes show the cross section view of the PCD, with a buffer depth of 0.5 m. Axes  $x$ ,  $y$ , and  $z$ , indicate easting, northing, and elevation, respectively. It can be noted a higher PCD porosity in **b**, than in **a**, corresponding to more sparse crops and lower AGB values.



## Field Based Destructive Measurements of Aboveground Carbon

In order to acquire reference values of biomass (i.e. ground-truth labels) to provide supervision to the ML regression algorithms, samples of AGB were systematically collected from the field at random locations during the growing season (locations shown in Figure 4 and resulting data sets, size and dimensions, are described in Table 1). The AGB sampling procedure followed the ICOS protocol for ancillary vegetation measurements [51] in 2020. During 2021, this AGB sampling procedure was modified, in order to maximize data sample size and quality, with a limited fieldwork capacity. Therefore, in 2021, at each location, three adjacent individual samples were collected. In total, three separate data sets of AGB were produced (Table 1).

An additional AGB dataset in 2021 was produced, composed of *augmented* samples. The augmentation procedure consisted of adding adjacent AGB samples, and their corresponding UAV-LiDAR data samples, so that both the AGB label and the LiDAR counterparts could be recalculated from the resulting combined sample. This augmentation scheme is shown in Figure 4 (c). This procedure allowed to produce one larger dataset (specifically, with 4/3 times more data samples) at a spatial resolution of 0.35-0.52  $m^2$  (cf. Revenga et al. 2022 [30] for a detailed explanation of the augmentation procedure).

We considered the plant carbon content in two separate parts: (i) aboveground and (ii) root carbon components ( $AGC$  and  $root_C$ , respectively). AGB was harvested and measured at randomized locations within the study site, according to ICOS protocols [51], throughout the two growing seasons (Figure 4 shows the sampling locations of AGB). Then, the AGB samples were oven-dried for 72h at 65°, to assess the dry biomass weight. The carbon content associated was measured by a laboratory appointed by the ICOS Ecosystem Thematic Center (ICOS ETC). The plant C content was evaluated as the C-to AGB ratio measured at 16 specific locations from the leaf tissue, where 45 g of tissue from the uppermost and middle-height leaves at each location were sampled. In this way, the C to-AGB ratio was determined as  $46.6 \pm 0.3\%$  in spring barley, and  $47.7 \pm 0.3\%$  in winter wheat.

The resulting reference AGC values were resampled to 1  $m^2$  resolution. In such way, we obtained a distribution of surface-based ground-truth estimates of AGC density at a spatial resolution of 1  $m^2$ . Table 1 provides a comprehensive overview of the sample count and spatial dimensions AGC reference labels in this study. The spatial distribution of the AGC sampling points is visualized in Figure 4 (b).

**Table 1.** Description of aboveground carbon (AGC) data sets. The subindex *aug.*, refers to the *augmented* dataset.

Growing season	Data set name	Number of samples	Sample dimensions (m)
2020	<i>barley<sub>20</sub></i>	104	1 x 0.35
2021	<i>wheat<sub>21</sub></i>	455	0.5 x 0.35
	<i>wheat<sub>21,aug.</sub></i>	609	(1-1.5) x 0.35

Additionally, we considered the amount of photoassimilated C not stocked as plant biomass or respired back into the atmosphere, but translocated to the soil as rhizodeposits (i.e.  $soil_C$ ). We relied on existing literature to estimate the C content translocated into the soil. In conventionally

219 managed crop fields,  $soil_C$  in sandy soils has been previously measured using  $^{14}C$  labelling and  
 220 reported as a relative fraction of GPP. Paush and Kuzyakov (2018) [52] report of a mean value  
 221 of 1.4% across 281 datasets including different crops and grasslands, while species-specific studies  
 222 report of 4-9% [53] and 2.2-2.9% [54] for wheat, and 0.4-2.4% [55] for barley.

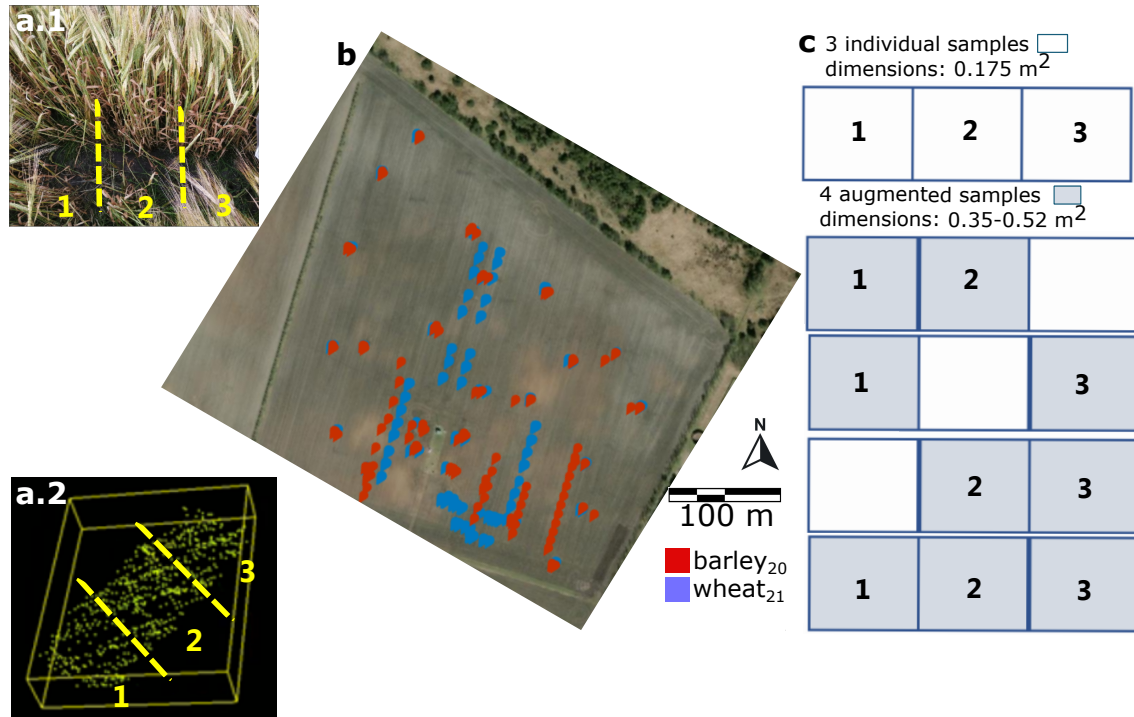


**Figure 4.** **a.1:** Three adjacent aboveground biomass samples (AGB) and the corresponding three LiDAR samples (**a.2**, dimensions of each sample:  $0.5 \times 0.35$  m). **b:** The spatial distribution of the AGB sampling locations. Each color indicates one of the original data sets: **red:** barley samples collected in 2020 (i.e. *barley*<sub>20</sub>); **blue:** wheat samples collected in 2021 (i.e. *wheat*<sub>21</sub>). **c:** dimensions of three original AGB samples (above), and data augmentation scheme by permutation (below); i.e. adding either two or three samples).

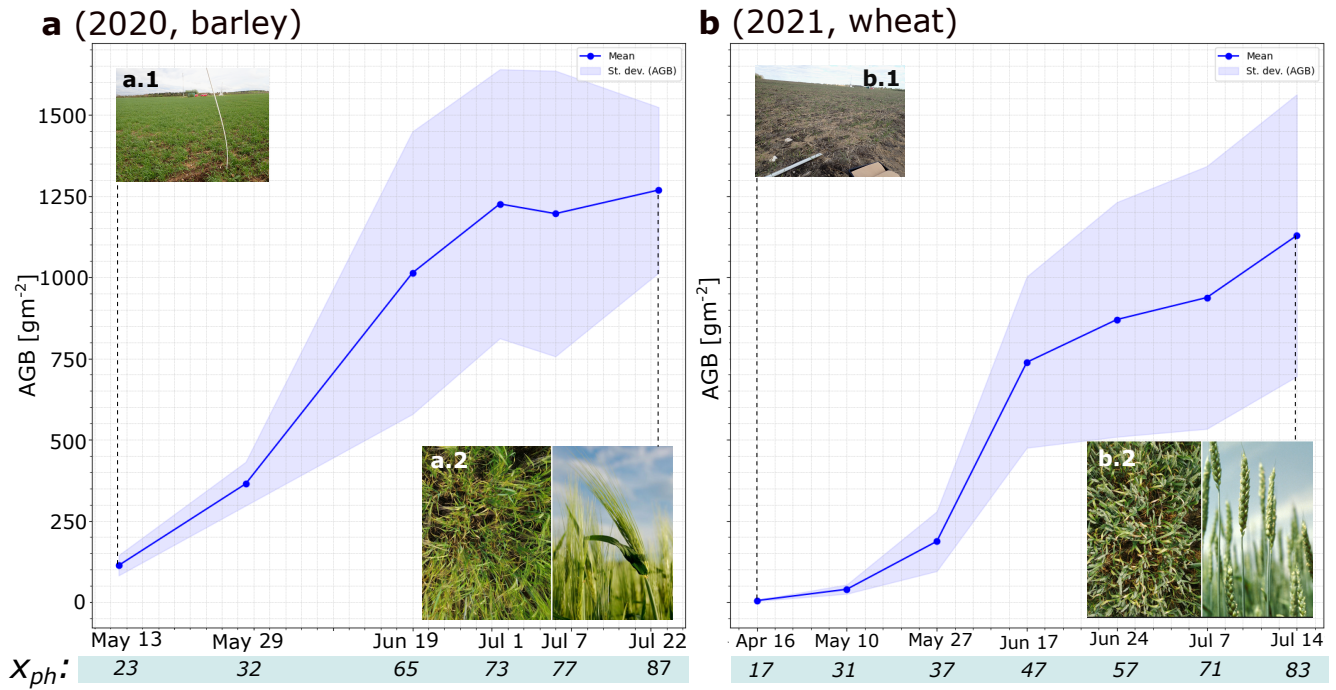


**Figure 5.** Crop development along the two growing seasons considered. Aboveground biomass (AGB) development during 2020 (a, barley) and during 2021 (b, wheat) growing seasons, respectively, indicating the dates of AGB sampling events. Y-axis indicates dry AGB matter. The blue solid line indicates the mean per sampling campaign, while the shaded area covers  $\pm$  the standard deviation. **a.1, a.2:** spring barley crop structure at the start of the sampling campaign and at maturity stage, respectively.  $x_{ph}$ : phenological growth stage (Zadoks decimal code) [56]. **b.1, b.2:** winter wheat crop structure at the start of the sampling campaign and at maturity stage, respectively. The AGB sampling during 2021 started earlier than in 2020, hence an initial value close to 0 at the start of the 2021 season.

## 223 Flux calculation

224 The study site is equipped with an eddy covariance (EC) system constituted of Gill HS-50 sonic  
 225 anemometers (Gill Instruments Ltd, Lymington, UK) and LI-7200RS enclosed infrared  $CO_2/H_2O$   
 226 gas analyzers (LI-COR, Lincoln, NE, USA) sampling at a frequency of 20Hz. The station is further  
 227 equipped for air- and soil-meteorological monitoring (air temperature: TA, relative humidity: RH,  
 228 air pressure: PA, global radiation, Rg, PPFd: photosynthesis active photon flux density, soil  
 229 temperature: TS, soil water content, SWC) with state-of-the-art instrumentation complying with  
 230 ICOS protocols for a class 1 ecosystem station [48].

## 231 Raw data processing

232 Raw 20 Hz wind,  $CO_2$ , water vapor, and sonic temperature data were processed utilizing  
 233 the EddyPro v. 7.0.9 software (LI-COR, Lincoln, NE). Half-hourly turbulent scalar fluxes were  
 234 calculated as the covariance between vertical wind speed and scalar variables (i.e.  $CO_2$ ,  $H_2O$ , T).  
 235 The processing included statistical tests for raw data screening [57], double coordinate rotation,  
 236 block averaging, time-lag optimization to maximize covariance, compensation for the effect of  
 237 density fluctuations on fluxes [58, 59], and low- and high-frequency spectral correction [60]. Half-



hourly turbulent scalar fluxes were calculated as the covariance between vertical wind speed and scalar variables (i.e. CO<sub>2</sub>, H<sub>2</sub>O, T). The raw data processing, quality control, and subsequent gap-filling procedures approximated the standards applied by ICOS ETC [48, 61]. The EC data produced at DK-Vng became part of the ICOS ETC database only in 2021. Therefore, in order to apply the same treatment to the two datasets (i.e. 2020 and 2021), we processed the raw data according to the ICOS ETC standards.

### ***Post-processing: Spike Removal, Quality Control, and Gap Filling***

During raw data processing and post-processing, low quality data were rejected leaving gaps in the dataset. This data screening consists of two sub-tasks: (i) an absolute limit test, that sets boundaries for a physically plausible range of values, and (ii) individual outliers were detected following the method proposed by Papale et al. (2006) [62]. Additionally, data were removed when the wind came from the direction of the instrumental plot (Figure 6, b).

During 2020's growing season, this resulted in a 56.8% of data rejected after all three filtering tests were applied. While the gaps occurred mainly at the beginning and end of the 2020 year (Autumn and Winter), the growing season was better populated with valid NEE data values. The data were gap-filled according the method proposed by Reichstein et al. (2005) [63], and the u\*-filtering procedure was based on season.

The processing of the 2021 flux data set followed the same procedure as for the 2020 season. The processed data showed a missing ratio of 32.9% after the quality control test and de-spiking, showing fewer gaps than the previous year and also a better flux data recording during the growing season.

To acquire a continuous dataset and allow to estimate *in situ* carbon budgets, data gaps were filled following the method of Reichstein et al. (2005) [63], using the [REddyProcWeb](#) tool. The method combines lookup tables of average fluxes under comparable meteorological conditions in a certain time window. If meteorological measurements are also missing, fluxes are estimated as the mean flux at the same time of the day in each time window (i.e. mean diurnal course).

### ***Estimation of Flux Climatology Footprint***

We calculated the flux climatology footprint using the model developed by Kljun et al. (2002) [64], and extracted the polygon covering the 70 % influence around the station (Figure 6, a).

In order to remove the influence of the instrumental plot surrounding the EC tower on the measurements, this area was masked out. For the 2020 dataset, the wind directions that covered the instrumental plot (18–198°) were excluded of further processing. The wind directions excluded in 2021 (18–116°) differed from the previous year due to a change in size of the instrumental plot. For this reason, in Figure 7, AGC maps show different shapes in each year.

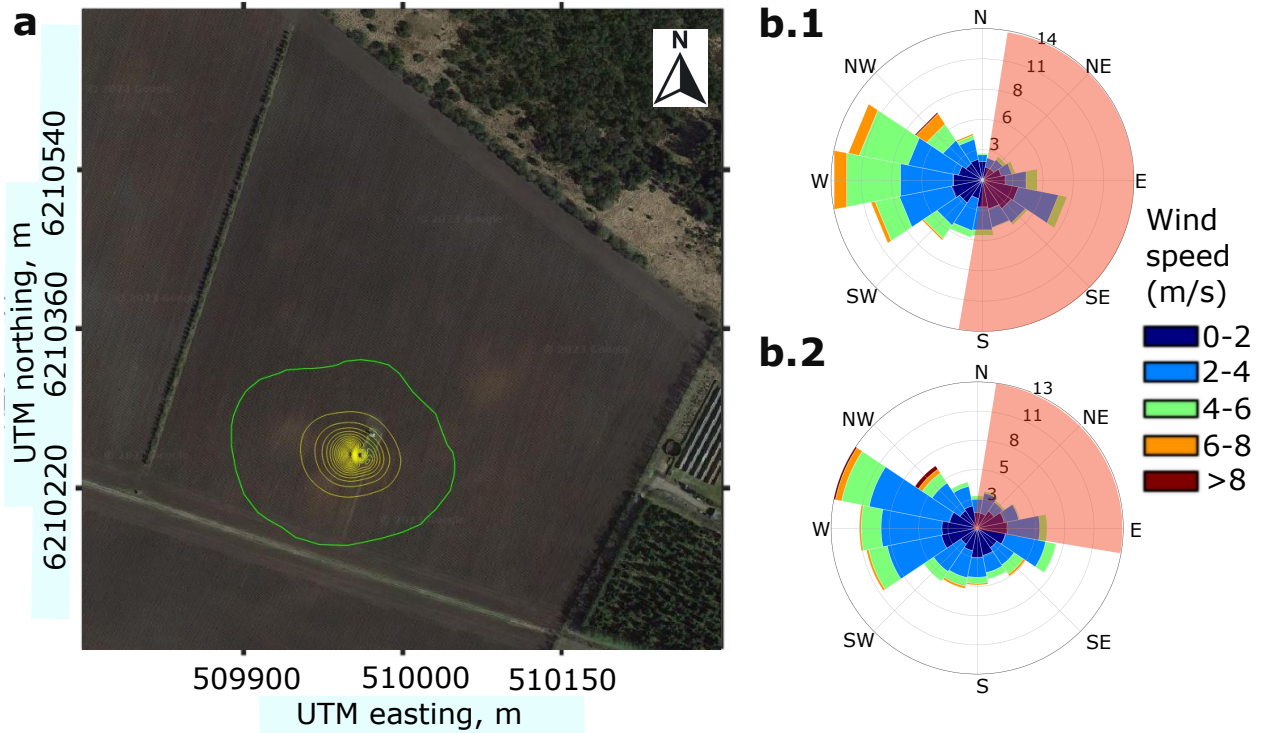


**Figure 6.** **a:** Flux footprint climatology map from the study site; the yellow contours indicate areas of 10 % increase of influence (source of background image: Google Earth 2023). **b.1, b.2:** wind frequencies at the study site during April–August of 2020 and 2021, respectively. The radius indicates total frequency of a given wind direction; the color indicates wind speed ( $\text{ms}^{-1}$ ). The shaded red areas cover the wind directions influenced by the instrumental plot—that were filtered out for flux analysis.

273

### *Ecosystem Flux Balance*

274

275

276

277

After data processing, the flux data sets provide an estimate of the net ecosystem exchange (NEE) (Figure 11, Appendix), allowing to estimate other NECB components. The estimation of net primary productivity (NPP) involved calculating the difference between NEE and ecosystem respiration. Therefore, we considered the flux balance

$$NPP = (-NEE) + R_h \quad (1)$$

278

279

280

where  $R_h$  accounts for the heterotrophic respiration, while  $R_a$  (i.e. autotrophic plant respiration) is contained within NPP. As per the usual convention, the negative sign indicates flux direction towards the ecosystem; the positive sign indicates a flux release towards the open atmosphere.

281

282

283

284

285

286

In conventional croplands (Figure 1), where the influence of higher-order heterotrophs (e.g. mammals, birds) can be considered negligible, the microbial soil respiration ( $R_{soil}$ ) constitutes  $R_h$ . Here, we modelled  $R_{soil}$  as a function of soil temperature during winter. Following Lloyd and Taylor (1994) [65], a second-order polynomial was fitted to the measurements of NEE prior to the start of the growing season (i.e. constituted of the  $R_h$  component only), as function of soil temperature 5 cm below surface. We filtered out  $R_{soil}$  values corresponding to frozen conditions

(i.e.  $< 0.5$  °C) for the model fit. Then, we extrapolated the modeled  $R_{soil}$  to the entire growing season. In 2020, as many datapoints were missing for  $T_{soil}$ , we filled the gaps with  $T_{air}$ , introducing a higher amplitude in the recorded values (therefore, also some added uncertainty in the estimate of NPP values).

## Machine Learning-based Carbon Estimates

### *Training, Evaluation and Validation of Predictions*

Three different ML regression models were initially selected for the task of AGC prediction. They were calibrated on a training dataset, and their performances were evaluated on a separate validation dataset; then, the best performing one was chosen for testing. This procedure helped avoid overfitting the model to the data, preventing an optimistically-biased accuracy assessment.

Therefore, we selected three fundamentally different ML methods; one representative of regularized linear models (i.e. Huber regressor [66, 67]), one tree-based ensemble method (i.e. Extreme Randomized Trees [68], ERT), and one exemplar from the boosting methods (i.e. Extreme Gradient Boosting [69]).

The model performance on the validation set was assessed via the average performance (indicated by the overbar) of the following metrics over ten randomized executions: coefficient of determination ( $\overline{R^2}$ ), mean squared error ( $\overline{MSE}$ ), mean absolute percentage error ( $\overline{MAPE}$ ), and mean absolute error ( $\overline{MAE}$ ). ERT obtained the best results across all four scores and therefore was selected as the model of choice. For more details on the model selection, validation and test procedure cf. Revenga et al. (2022) [30].

### *Description of the Model Selected*

Extremely Randomized Trees (ERT) is an ensemble learning technique that aggregates the results of multiple individually created decision trees to output regression results [68]. It is originally derived from the Random Forest model [70]. In an ERT model, every individual predictor—i.e. a binary decision tree—of an ERT is constructed from the whole training set. A single tree decides at each node, which split of a random subset of features splits reduces the reconstruction error (e.g. MAE or MSE) the most. The random sampling of features and the random splits within the features range leads to more diverse and thus less correlated decision trees, thereby leading to improved generalization results. Each tree is considered to be a “weak” regressor performance-wise but the combination creates an ensemble that outperforms the individual regressors. As final prediction, the average predictions of the individual decision trees in the forest is used, providing an estimate of above ground carbon (i.e.  $\widehat{AGC}$ ).

## Aboveground and Root Carbon Estimates

Using the AGB prediction results (Figure 7), and the C-to-biomass ratio measured, we calculated the total AGC within each EC footprint. Then, the total plant C estimates were obtained by calculating at each point the total plant C derived from the AGC prediction. In order to obtain this estimate, we considered the allocation of C below ground as a function of the phenological stage using Eq. 2 (Figure 8), fixing  $root_C$  at anthesis as  $10 \pm 1\%$  of total plant C at maturity of crops, according to reference literature [71]. Therefore,  $root_C$  was calculated as a function of

326 (i) AGC, (ii) the rate at which GPP is translocated to the roots ( $GPP_{roots}$ ) [72], and (iii) the  
 327 phenological stage (i.e.  $x_{ph}$ ) [56]:

$$root_C(x_{ph}) = \begin{cases} x_{ph} \cdot GPP_{roots}, & \text{if } x_{ph} < x_{anthesis} \\ (0.1 \pm 0.01) \cdot AGC_{mat}, & \text{if } x_{ph} = x_{anthesis} \\ root_{C,post}(x_{ph}), & \text{if } x_{ph} \geq x_{anthesis} \end{cases} \quad (2)$$

328 where  $AGC_{mat}$  indicates aboveground carbon at maturity stage; the function  $root_{C,post}(x_{ph})$   
 329 was defined by a linear fit to  $root_C$  at anthesis and values of  $GPP_{roots}$  in literature at each growth  
 330 stage, for wheat and barley in sandy soils, respectively [72]. Similarly,  $GPP_{roots}$  was obtained as  
 331 the slope of a linear fit between the onset of the season and  $root_C$  at anthesis.

332 Likewise,  $soil_C$  at each date was calculated as a linear fit to the values reported in literature  
 333 of  $^{14}C$  pulse-labelling for barley [54] and wheat [73] in sandy soils. This resulted on an average  
 334 translocation of GPP to rhizodeposits of 2.73% and 1% for barley and wheat, respectively.

335 = **Results** =

336 **Plant Carbon Maps**

337 We selected nine UAV-LiDAR survey dates (five during 2020; four during 2021), and inter-  
 338 sected them with the 70 % of the area of influence surrounding the eddy-covariance station. For  
 339 each UAV-LiDAR survey in 2020 and 2021, we created a map of AGB at 1m<sup>2</sup> spatial resolution  
 340 (following the procedure described in Revenga et al., 2022 [30]).

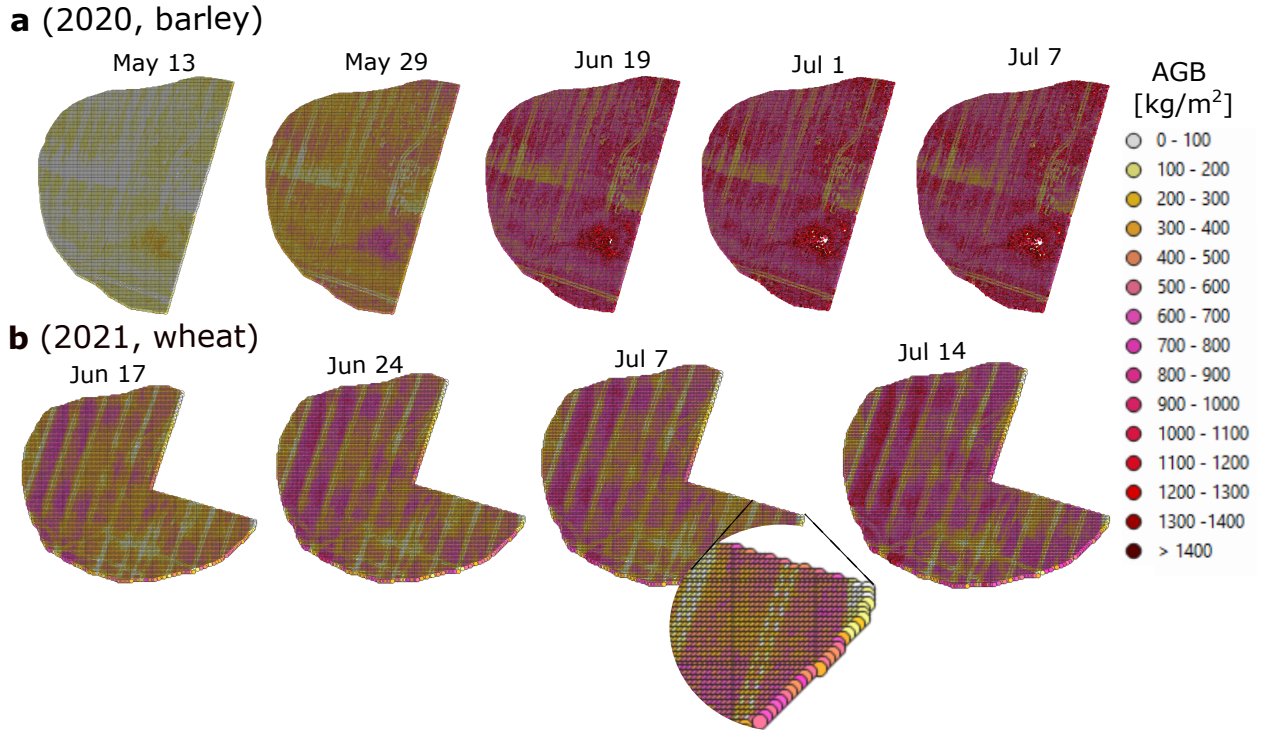


**Figure 7.** Exemplary aboveground biomass (AGB) maps. **a:** 2020 growing season; **b:** 2021 growing season. Values in legend indicate predictions of dry AGB matter. A sector of the eddy-covariance station footprint was clipped out to avoid influence from the instrumental plot on the results: in 2020, the (18–198)° wind directions were excluded; in 2021, the wind directions (18–116)° were excluded.

341 ***Above- and Belowground Carbon Estimates***

342 In 2020, the AGB collection campaign started at a level of 100 gm<sup>-2</sup> of AGB. In Figure 5  
 343 (a) it can be observed a steady linear increase until 1 July, where there is a turning point, and  
 344 a saturation plateau afterwards. From then onward, AGB stabilizes, i.e. by the harvesting date  
 345 (end of July), the AGB are just slightly above the one measured on 1 July.

346 In contrast, in order to extend the span of AGB measurements, during the 2021 campaign the  
 347 AGB sampling started at a point slightly above 0 gm<sup>-2</sup>, where can be noted a slow start of AGB  
 348 accumulation. By approximately the same date (27 May), the AGB in 2021 growing season lags  
 349 150 gm<sup>-2</sup> behind the previous year. This can be compared with the NEE of both years (Figure  
 350 11, in Annex) showing a "false start" in 2021 11 (b), so until start of June NPP barely offsets R<sub>eco</sub>.  
 351 Instead of saturating by 1 July, AGB kept growing until the last sampling date. This observation

352 was expected, considering that the crops in 2021 exhibited a time-lag of approximately 15 days  
353 compared to the previous year (see Figures 11 and 12, in Annex).

354 The difference in AGB between the two years translates linearly to differences in AGC by  
355 modeling C content to be constant across all plant tissue ( $46.6 \pm 0.3\%$  in barley, and  $47.7 \pm 0.3\%$   
356 in wheat). Notably, wheat moves a greater amount of photoassimilated C below ground compared  
357 to barley, in relative terms. This different strategy becomes increasingly evident as the growing  
358 season progresses and becomes particularly apparent at the maturity stage.

359 The difference between the measured AGC in both growing seasons (i.e.  $\approx 235 \text{ gm}^{-2}$  more in  
360 2020 than in 2021) can be attributed to the harsher environmental conditions that the 2021 crops  
361 endured at the beginning of the season, causing a delay and a sparser structure (Appendix).



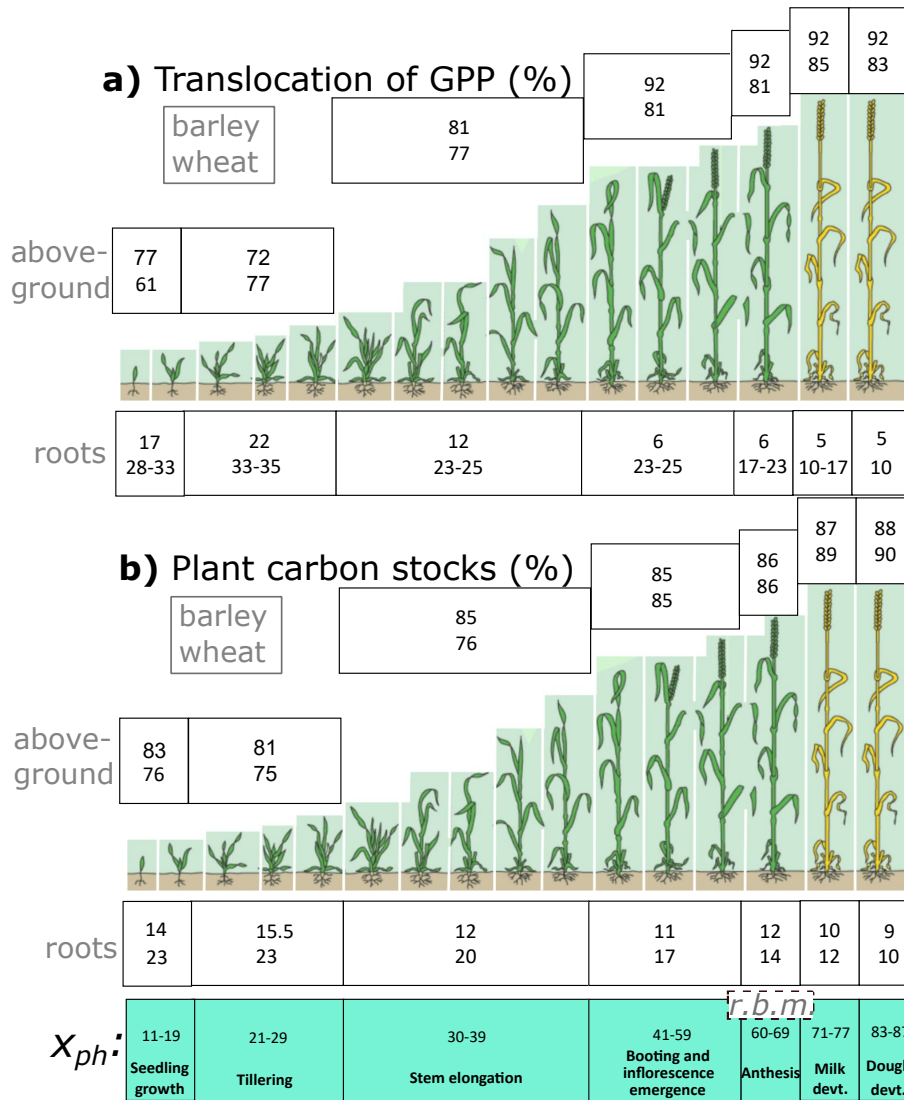


**Figure 8.** **a:** Translocation of photoassimilated atmospheric carbon (i.e. GPP) to aboveground and root components (rhizodeposits are not included); values in white boxes indicate estimated % corresponding to the same phase. **b:** Plant carbon stocks along the growing season showing the estimated carbon allocation at each phenological stage (adapted from [74]). Percentage values of carbon in roots (both translocated and stocks) are derived from [72] for wheat and barley crops in sandy soils. Each white box shows values for spring barley (above) and winter wheat (below).  $x_{ph}$ : phenological growth stage (Zadoks decimal code) [56]. The inset indicating r.b.m. shows the stage when the root biomass maximum occurs.

### Carbon fluxes from the eddy-covariance method

The cumulative NPP curves of the two growing seasons considered are shown in Figure 9. the progression of the curve in the year 2020 exhibits saturation by the terminal data collection (i.e. on July 22), whereas in the subsequent year, 2021, the ultimate survey (i.e. July 14) coincides with a phase characterized by the ongoing ascendant trajectory of the net ecosystem's uptake.

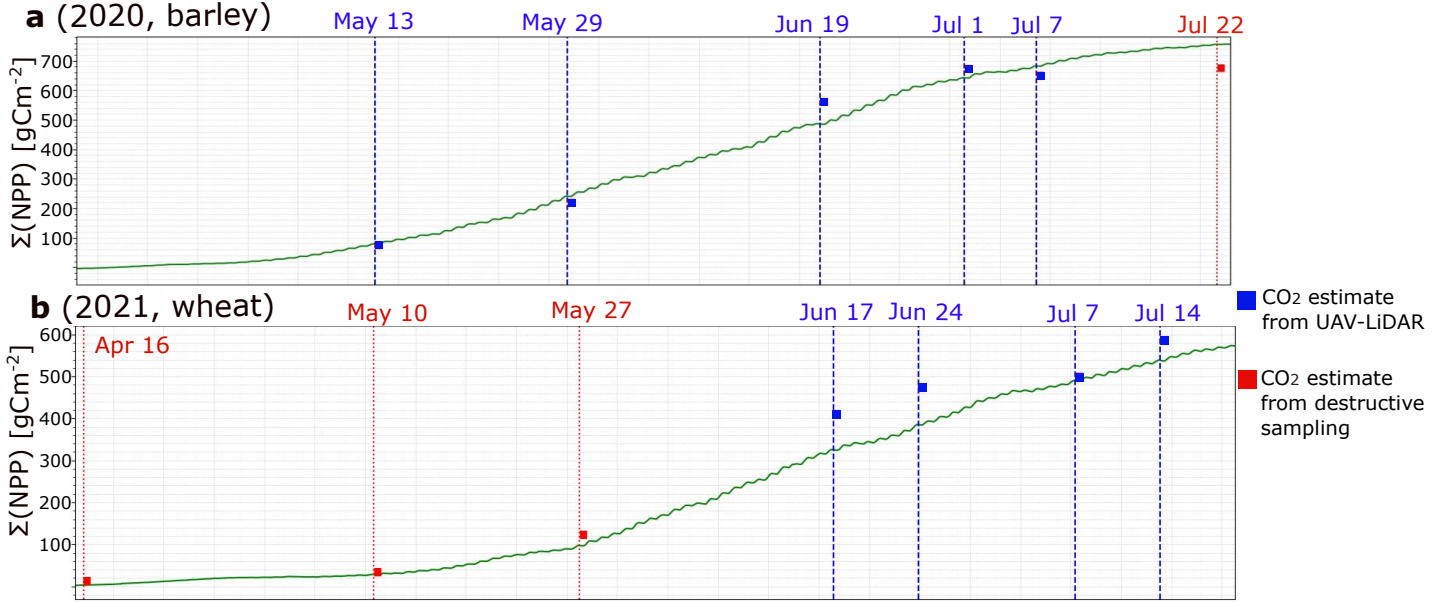


**Figure 9.** Cumulative NPP (gCm<sup>-2</sup>) along (a) the 2020 and (b) the 2021 growing seasons. The red dotted vertical lines indicate aboveground biomass (AGB) sampling dates, while the blue dashed lines indicate dates in which both AGB sampling and UAV-LiDAR surveys took place. The square marks indicate the plant-C estimates for a given date using the UAV-LiDAR method (blue dates), or based on C estimated from destructive sampling (red dates).

### Comparing Flux Data and UAV-based Plant Carbon Estimates

Table 2 shows the results of the plant carbon estimates via the UAV-LiDAR method against the cumulative partitioned fluxes estimated via the eddy-covariance method.

In order to quantify the degree of over- or underestimation that the UAV-LiDAR-based method produces with respect to the cumulative NPP, we used the following metric, referred to as delta-ratio ( $\Delta_C$ ). It is defined as the ratio between the increment of plant C and the increment in NPP between two separate surveying dates:

$$\Delta_C = \frac{\Delta(NPP_{i,j}) - \Delta(PlantC_{i,j})}{\Delta(NPP_{i,j})} \cdot 100 \quad (3)$$

where the subindexes  $i, j$  refer to two different surveying dates.



**Table 2.** Results of carbon estimates via the two independent methods considered. The first column indicates the UAV-LiDAR survey dates; second and third columns show the plant carbon stock estimated via the UAV-LiDAR method (both AGC and  $root_C$ ); the last three columns show the cumulative values (from the start of the photosynthetic season) of the ecosystem flux components partitioned into net ecosystem exchange (NEE), heterotrophic respiration  $R_h$  and net primary productivity (NPP).  $x_{ph}$  indicates the average phenological growth stage (Zadoks decimal code) [56] measured at 12 control plots.  $soil_C$ : rhizodeposits.

Method		UAV-LiDAR			Eddy-covariance		
d/m/yyyy	$x_{ph}$	AGC [ $gm^{-2}$ ]	$root_C$ [ $gm^{-2}$ ]	$soil_C$	-NEE [ $gCm^{-2}$ ]	$R_h$ [ $gCm^{-2}$ ]	NPP [ $gCm^{-2}$ ]
13/5/2020	23	52.4	8.9	1.72	35.7	143.4	91.0
29/5/2020	32	168.8	32.0	5.63	81.9	237.9	252.5
19/6/2020	65	469.3	65.2	15.0	286.1	423.0	497.7
1/7/2020	73	567.5	75.1	18.0	401.4	533.1	653.8
7/7/2020	77	553.6	66.4	17.4	423.6	577.7	693.7
22/7/2020	87	587.3	58.7	18.1	463.4	681.8	767.6
16/4/2021	17	2.3	0.7	0.0	83.6	90.7	0.9
10/5/2021	31	18.4	5.5	0.3	147.6	100.8	25.5
27/5/2021	37	86.7	25.8	1.1	68.6	229.5	94.5
17/6/2021	47	341.9	55.5	4.0	102.5	418.4	321.3
24/6/2021	57	402.7	58.0	4.7	144.3	482.0	372.5
07/7/2021	71	434.1	50	4.9	227.3	592.1	486.1
14/7/2021	77	522.6	48.5	5.8	251.5	672.1	532.0

**= Discussion =**

This study presents a comparison of two independent methods to estimate C uptake in managed croplands. We assessed a method that utilizes UAV-LiDAR technology to derive C dynamics in croplands by surveying the ecosystem along two growing seasons, covered by barley (in 2020) and wheat (in 2021). The results obtained compare favorably with respect to the cumulative NPP when the first UAV-LiDAR survey date is taken early in the growing season; conversely, comparisons lose consistency when time intervals between surveying dates are short, concurrently with a late phenological stage.

**Plant Carbon Components: Values and Uncertainty**

The uncertainty estimate of the AGC component was derived from the AGB sampling technique, because, assuming a constant ratio of AGB:C, the uncertainty on the lab analysis (i.e.  $\pm 1\%$  of C-to-AGB ratio) is comparatively negligible with respect to the AGB uncertainty (i.e. AGB label noise). While certain studies report of uneven C-to-AGB ratios along the plant components—specially seeds and grain-bearing organs—[...], we assumed this ratio to stay relatively constant across the plant components. We consider AGC as the component most accurately assessed between the above- and belowground components.

Management practices and environmental factors affect the BGB-to-AGB allometric ratio in cereal crops (e.g. root depth is function of soil moisture content) [...], therefore such BGB estimates are usually prone to bias or uncertain [71].  $root_C$  is much depending on availability of water,

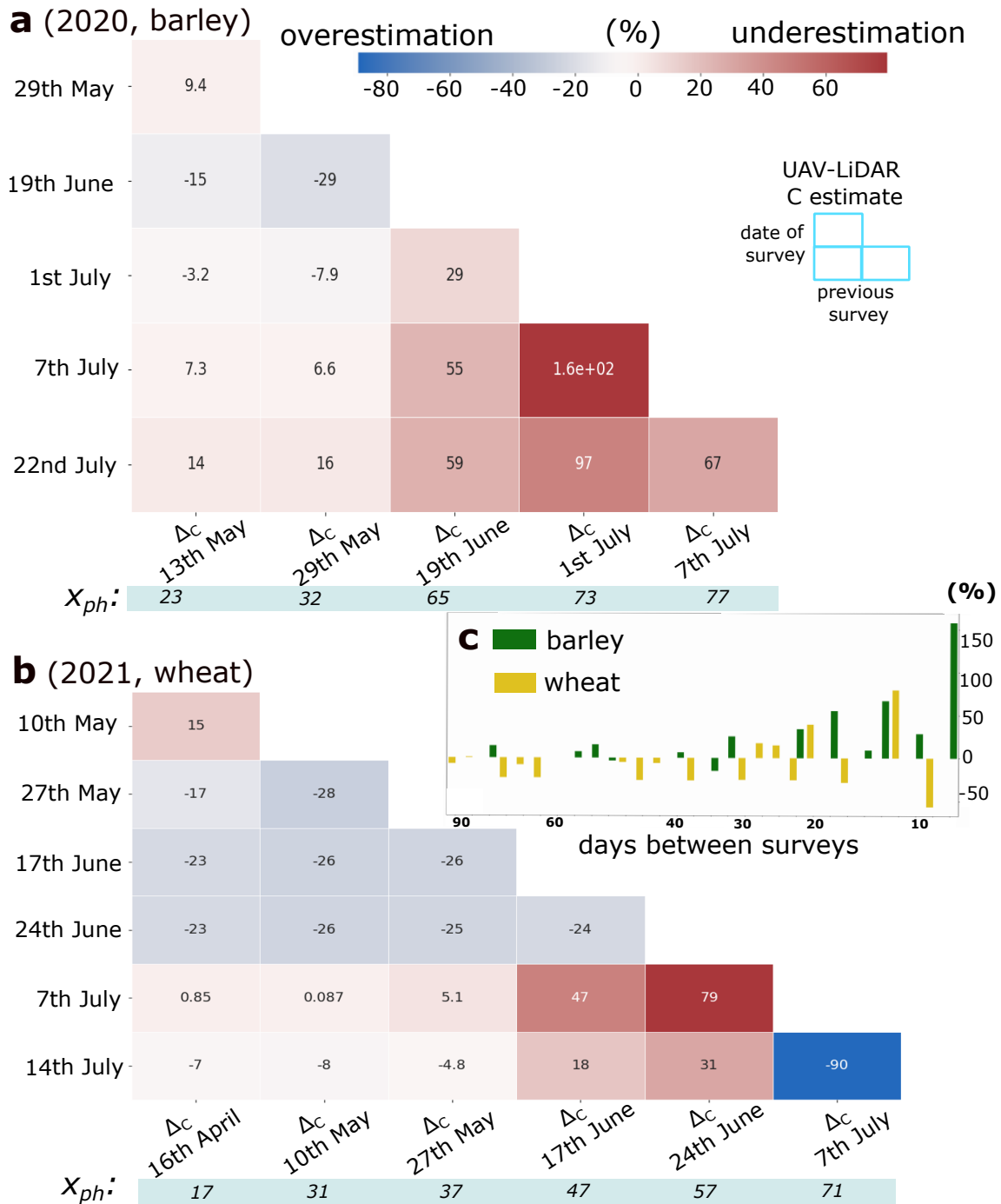


**Figure 10.** Carbon delta-ratio ( $\Delta_C$ ) values between pairs of surveying dates during the 2020 (a) and 2021 (b) growing seasons; the reference ( $\Delta_C = 0$ ) is the cumulative NPP at a given date. The inset (c) shows the error distribution along the time between UAV-LiDAR survey dates for both crop types. It can be noted that (i) LiDAR estimates become more in agreement with NPP as time between surveys increases, and that (ii) considerable over- and underestimates are found between closely spaced dates during a late phenological stage (right tails of both a and b tables).  $x_{ph}$  indicates the average phenological growth stage.

394 nutrients and nonstructural carbohydrates [...]. Moreover, there is high variability in  $root_C$  along  
 395 the growing season, increasing towards the flowering period (i.e. anthesis), and then gradually  
 396 decreasing towards maturity ([72]), as nutrients are dynamically allocated to the upper parts  
 397 during the last crop development, sourcing from the roots. Here, following Hu et al. (2018) [71],  
 398 we estimated the BGB at anthesis (which corresponds to the root biomass maximum in Figure 8),  
 399 as given by the ratio  $\frac{root_C}{(AGC+root_C)} = 0.10 \pm 0.01$ . This ratio relates AGC (at maturity) and  
 400  $root_C$  (at anthesis, standardized to 25 cm depth). It holds for conventional farming systems and  
 401 is also supported by findings of Chiranda et al. (2012) [75]. The phenological growth stage [51]  
 402 indicating anthesis (Zadok's decimal code of plant development = 65) [56] was observed on 18 June  
 403 2020. In 2021, the anthesis stage was not recorded, but based on field image documentation, was  
 404 estimated to correspond to 1 July 2021. Following this ratio, and the rate of photoassimilated C  
 405 translocated to roots for barley and wheat in sandy soils [72], we estimated the  $root_C$  component  
 406 at each biomass sampling date. We acknowledge that variations in season-specific environmental  
 407 conditions can lead to differences in such ratios [...]. Therefore, one of the limitations of our method  
 408 lays on the fact that we estimate per-component C stocks as if they in fact distribute C as reported  
 409 in the existing literature for the same crops under similar conditions.

410 Provided that the Hu's ratio [71] is robust and applicable to the environmental conditions of  
 411 our study, the results presented in this study are therefore most limited with respect to the design  
 412 of the AGC sampling campaigns for each individual date.

413 Our sampling design was conceived to optimize predictability of AGC from the PCD data,  
 414 however, our sampling design turned out to be suboptimal for the application of comparing entire  
 415 plant C and flux-based estimates on individual dates. Ideally, for the task of intercomparison of  
 416 C stocks, at every date the locations for AGC sampling should be entirely randomized, across an  
 417 area which is (i) large enough, and (ii) either within the flux tower footprint or representative of  
 418 the vegetation traits contained within the footprint.

419 However, in specific dates, it was found to be advantageous for predicting *in situ* AGC to  
 420 collect data from locations with contrasting AGB values. This approach allowed us to capture the  
 421 two-dimensional variability of AGC corresponding to the observed variations in the PCD scene.  
 422 While this procedure facilitates the establishment of an empirical relationship between covariates  
 423 (i.e. height metrics derived from PCD) and the response variable (i.e. AGC), it compromises the  
 424 comparability of cumulative fluxes on particular dates. Consequently, it may lead to apparent  
 425 over- or underestimation of plant carbon stocks derived from UAV-LiDAR data in relation to net  
 426 primary productivity (NPP). In both years, this is particularly evident in the comparison of  $\Delta_C$   
 427 stocks when the 7th of July is involved (Figure 10).

428 From Table 2, it can be observed how, on 7 July 2020, the AGC sample is 14 g lighter than the  
 429 previous survey date (i.e. 1 July), while the cumulative NPP for the corresponding time period  
 430 exhibits an increase of approximately 40 g. This corresponds to a decreasing LiDAR-derived  
 431 plant-C estimate between these two dates (Figure 9, a). This disagreement can only be attributed  
 432 to the inherent bias introduced by the sampling procedure, thereby highlighting the significant  
 433 impact of the sampling design on the resulting outcome. Ideally, during each AGB sampling date,  
 434 data collection should be completely randomized, without intervening explicitly to ensure AGC  
 435 variability.

436 On certain dates, the presence of sample selection bias [76, 77] introduced by the aforemen-  
 437 tioned approach resulted in inconsistency when comparing plant C values with flux-based cumula-  
 438 tive carbon estimates. This is a reasonable outcome, as the continuous flux-based carbon estimates  
 439 are unaffected by the AGC sampling design.

### 440 Ecosystem Carbon-Uptake Derived from Flux Data

441 A limitation of our approach rests on the fact that  $R_h$  was modeled as function of soil tempera-  
 442 ture, taking as sample data to model  $R_{soil}(T_{soil})$  the dates prior to the onset of the photosynthetic  
 443 season (i.e. December–February). During these dates, temperatures did not span a wide range.  
 444 Therefore, the low dynamics in the values of soil temperature during the beginning of the year may  
 445 lead to underestimations in the modeled  $R_h$ . Accurately modeling heterotrophic soil respiration  
 446 ( $R_h$ ) as a function of temperature may be challenging, particularly when the range of temperatures  
 447 before shoot emergence (i.e. onset of photosynthetic season) is narrow. This can lead to uncertainties  
 448 in the predicted values of  $R_h$ . In order to narrow it down, further studies should consider combining  
 449 the setup we employed with flux chambers.

450 The exact dates of fertilizer deposition by the farmer remain unknown. The effect of such  
 451 field managemet (e.g. fertilizer application, irrigation) cannot be reflected i nhe LiDAR derived C  
 452 estimates, but do have an impact on the measured fluxes.

### 453 Comparing Flux Data and UAV-based Plant Carbon Estimates

454 Figure 10 shows the result of the comparison of C stocks obtained via the two independent  
 455 methods, as delta values ( $\Delta_C$ ). Several observations can be made:

- 456 • (i) The optimal reference date for comparing an increase of plant C stocks is the first date,  
 457 at the beginning of the growing season. This observation applies to both years.
  - 458 – When the 1<sup>st</sup> date is the reference, the mean error of predictions in 2020 shows:  $2.5 \pm$   
 459  $10.4$  % while in 2021 the mean error is  $-9.0 \pm 13.3$  %.
  - 460 – When taking as reference the 2<sup>nd</sup> date, in 2020 the match between both independent  
 461 estimates shows a mean error of  $-3 \pm 16.9$  %. Likewise, in 2021 the mean error is:  $-8.9 \pm$   
 462  $11.4$  %.
  - 463 – When considering the 3<sup>rd</sup> date as the reference, the findings indicate a persistent un-  
 464 derestimation of  $47.6 \pm 13.3$  % in 2020, whereas the results for 2021 exhibit a closer  
 465 approximation to the reference NPP value, with a deviation of  $-12.7 \pm 13.3$  %.
- 466 • (ii) The right tail ends of both tables show that comparing close dates at a late phenological  
 467 stage results in evident over- and underestimations. So, in addition to the temporal proximity  
 468 of survey dates, the phenological stage of the crops appears to exert a significant influence.
- 469 • (iii) The included inset panel (c) presents the  $\Delta_C$  values of both crops, along the temporal  
 470 interval between survey dates. A clear trend can be observed, indicating a consistent increase  
 471 in errors as the UAV-LiDAR survey dates approximate.

472 Figure 12 (in Appendix) shows the cumulative values of  $R_{eco}$ , NPP, and GPP, in both growing  
 473 seasons. It can be observed how the C uptake does not offset respiratory ecosystem losses until  
 474 the 4<sup>th</sup> of June. This represents a time shift with respect to 2020 of 15 days, where the crossing

475 of GPP and  $R_{eco}$  occurred in 19<sup>th</sup> of May. This seemingly time lag during the initial stages of  
 476 the growing season appears to have manifested as a significant temporal displacement of the entire  
 477 crop phenological process, estimated to be approximately of 15 days. This temporal shift can  
 478 be visualized by comparing the time discrepancy in the emergence of the uplifting point in NPP  
 479 between panels a and b in Figure 9.

480 UAV-based remote sensing is being increasingly applied to assist in ecosystem fluxes analysis  
 481 due to the ability of UAV-borne sensors to capture changing land surface variables as well as  
 482 their spatial distribution [26]. The combination of EC towers with UAV-based remote sensing  
 483 shows potential for estimating ecosystem fluxes in areas where observational gaps exists, due to  
 484 lack of monitoring capacity or difficult accessibility. Moreover, there is an interest in developing  
 485 independent methods to estimate the same ecosystem variable (i.e. NECB), in order to target  
 486 sources of uncertainty, and advance existing techniques.

487 In this study, the observed disparities between the two methods considered improve the un-  
 488 certainty reported in previous studies between modeled and empirical approaches to estimate C  
 489 stocks in croplands. For instance, a 18% of discrepancy between modeled and observed crop mass  
 490 is reported by Soltani et al. (2012) [78]. However, we consider that the most noteworthy aspect of  
 491 the proposed method is its ability to provide flexible estimates of carbon fluxes that align well with  
 492 the EC flux estimates. Furthermore, these estimates can be obtained without reliance on ground-  
 493 based instrumentation, enabling the assessment of ecosystems that are otherwise inaccessible or  
 494 poorly documented.

## 495 = Conclusions =

496 Total plant-mediated C stocks can be accurately estimated using UAV-LiDAR in combination  
 497 with machine learning regression methods at the ecosystem scale. These estimates correspond to  
 498 cumulative CO<sub>2</sub> fluxes uptaken during the crop development. The match between the temporal  
 499 development in C uptake in the footprint of the EC tower using the UAV-LiDAR based method  
 500 and the eddy-covariance estimates showed an optimal mean error of  $2.5 \pm 10.4$  % (in spring barley),  
 501 and of  $-9.0 \pm 13.3$  % (in winter wheat), finding that the comparisons of C stocks over the entire  
 502 growing season (i.e. considering the first survey as reference date) resulted to be the most accurate  
 503 ones.

504 However, it is crucial to consider that UAV-LiDAR estimates of C uptake may exhibit sub-  
 505 stantial over- or underestimation under certain conditions. This can occur when (i) LiDAR surveys  
 506 are too close to one another, particularly during the later stages of phenological development, and  
 507 (ii) a sample selection bias is introduced. For instance, it can be noted a positive bias on the 17  
 508 and 24 June 2021 (Figure 9), resulting in consistent overestimations in any comparison where these  
 509 two dates are considered (Figure 10, b). Therefore, care must be taken as regards allowing suitable  
 510 time intervals between surveys and appropriate AGC sampling schemes.

511 When comparing the resulting plant-C values with eddy-covariance estimates, a satisfactory  
 512 level of agreement is observed, provided that the effects of AGC sampling design and time interval  
 513 between UAV-LiDAR survey dates are taken into account. Conversely,  $root_C$  is highly influenced by  
 514 management practices and environmental factors throughout the growing season. Consequently,  
 515  $root_C$  contributes significantly to the uncertainty in plant carbon estimates derived from UAV-  
 516 LiDAR data.

517 We consider these results a promising step towards the data-driven upscaling of directly mea-  
 518 sured fluxes during the growing season in managed ecosystems, as well as towards the interpolation  
 519 of CO<sub>2</sub> fluxes across eddy-covariance stations by leveraging mobile platforms and LiDAR technol-  
 520 ogy.

### 521 = Author contributions =

522 Original conceptual framework: TF, KT, JCR; methodology: JCR; experimental design: KT,  
 523 TF, JCR; UAV-LiDAR data collection: JCR, KT; field-based data collection and curation: RJ,  
 524 JCR, KT; laser data processing: JCR, KT; eddy-covariance data collection and processing: RJ, TF,  
 525 JCR; feature engineering, machine learning models' training and evaluation: JCR; visualisation:  
 526 JCR and PR; project supervision: TF, KT; project administration: TF, KT; writing—original  
 527 draft preparation: JCR; writing—review and editing: JCR, PR, TF, KT.

528 All contributing authors have read and agreed to the published version of the manuscript.

### 529 = Acknowledgements =

530 The authors acknowledge the contributions of René Lee, Lars Rasmussen, Rune Skov Mai-  
 531 goord, Binsheng Gao, and Alek Wieckowski, in supporting the tasks of field data acquisition,  
 532 contributing to this study as fieldwork and laboratory assistants.

### 533 = Funding =

534 This project has received funding support from the Talent Program Horizon 2020/Marie  
 535 Skłodowska-Curie Actions, a Villum Experiment grant by the Velux Foundations, DK (MapCland  
 536 project, project number: 00028314), the DeepCrop project (UCPH Strategic plan 2023 Data +  
 537 Pool), as well as a UAS- ability infrastructure grant from Danish Agency for Science, Technology  
 538 and Innovation. The authors acknowledge as well financial support from ICOS.

### 539 List of abbreviations

- 540 • AGB: aboveground biomass.
- 541 • AGC: aboveground carbon.
- 542 • EC: eddy-covariance.
- 543 • ECB: ecosystem carbon balance.
- 544 • ERT: extreme randomized trees.
- 545 • GHG: greenhouse gas.
- 546 • GPP: gross primary productivity.
- 547 • ICOS: integrated carbon observation system.
- 548 • LiDAR: light detection and ranging.
- 549 • ML: machine learning.
- 550 • NECB: net ecosystem carbon balance.
- 551 • NEE: net ecosystem exchange.
- 552 • NPP: net primary productivity.
- 553 • PCD: point cloud data.

- 554 •  $R_a$ : autotrophic plant respiration.
- 555 •  $R_{eco}$ : ecosystem respiration.
- 556 • RF: random forest.
- 557 •  $R_h$ : heterotrophic respiration.
- 558 •  $root_C$ : carbon content in roots.
- 559 •  $R_{soil}$ : microbial soil respiration.
- 560 • RS: remote sensing.
- 561 •  $soil_C$ : soil rhizodeposition.
- 562 • UAV: unstaffed aerial vehicle.
- 563 • WDI: water deficit index.
- 564 •  $X_{ph}$ : crops growth stage (according to Zadoks decimal code).

### 565 **Annex I: NEE, NPP, GPP, $R_{eco}$ in both growing seasons (2020 and 2021)**

566 Figure 11 displays the processed NEE over time for both years, with a 30-minute pixel res-  
 567 olution. It can be noted that in the 2020 season, there was an advancement of approximately 15  
 568 days, and more concentrated C uptake hotspots between 11:00 and 14:00 in late June and late  
 569 July compared to the 2021 season.

570 Remarkably, in Figure 12, it can be observed that the time series of cumulative NPP and  $R_{eco}$   
 571 never cross each other in 2021 (b), while they do so in 2020 (a). The enclosed area under these  
 572 two curves indicates the rate of C accumulation efficiency with respect to ecosystem respiratory  
 573 losses. It makes sense that in a more homogeneous, densely populated crop, the C uptake was  
 574 more efficient than in the sparse crops of 2021.

575 These observations are consistent with the AGC sampling campaigns—where more sparse  
 576 crops were sampled in the second year—and with the PCD representation of the cropfields (Figure  
 577 3)—where a higher PCD porosity was found in the second year as well as a lower cumulative NPP  
 578 flux (Figure 9).

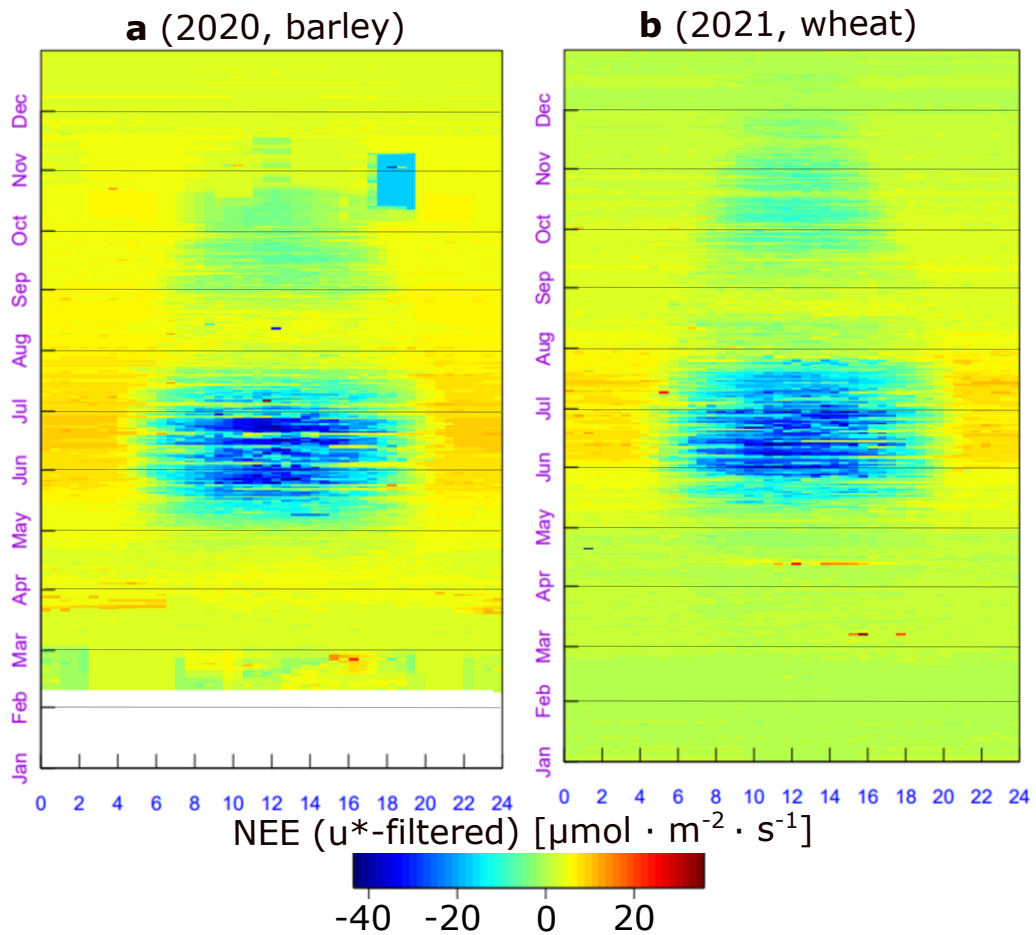


**Figure 11.** Measured net ecosystem exchange (NEE) at Voulundgaard research station during 2020 (a) and 2021 (b). Data displayed were gap-filled, spikes removed and  $u^*$ -filtered. It can be noted a delay in the onset of the growing season in 2021 with respect to 2020 of almost 3 weeks, including a false start in mid May, partly explained by the cold spell of 10-12<sup>th</sup> February (figure obtained from the REddyProcWeb online tool : [www.bgc-jena.mpg.de/bgi/index.php/Services/REddyProcWeb](http://www.bgc-jena.mpg.de/bgi/index.php/Services/REddyProcWeb)).



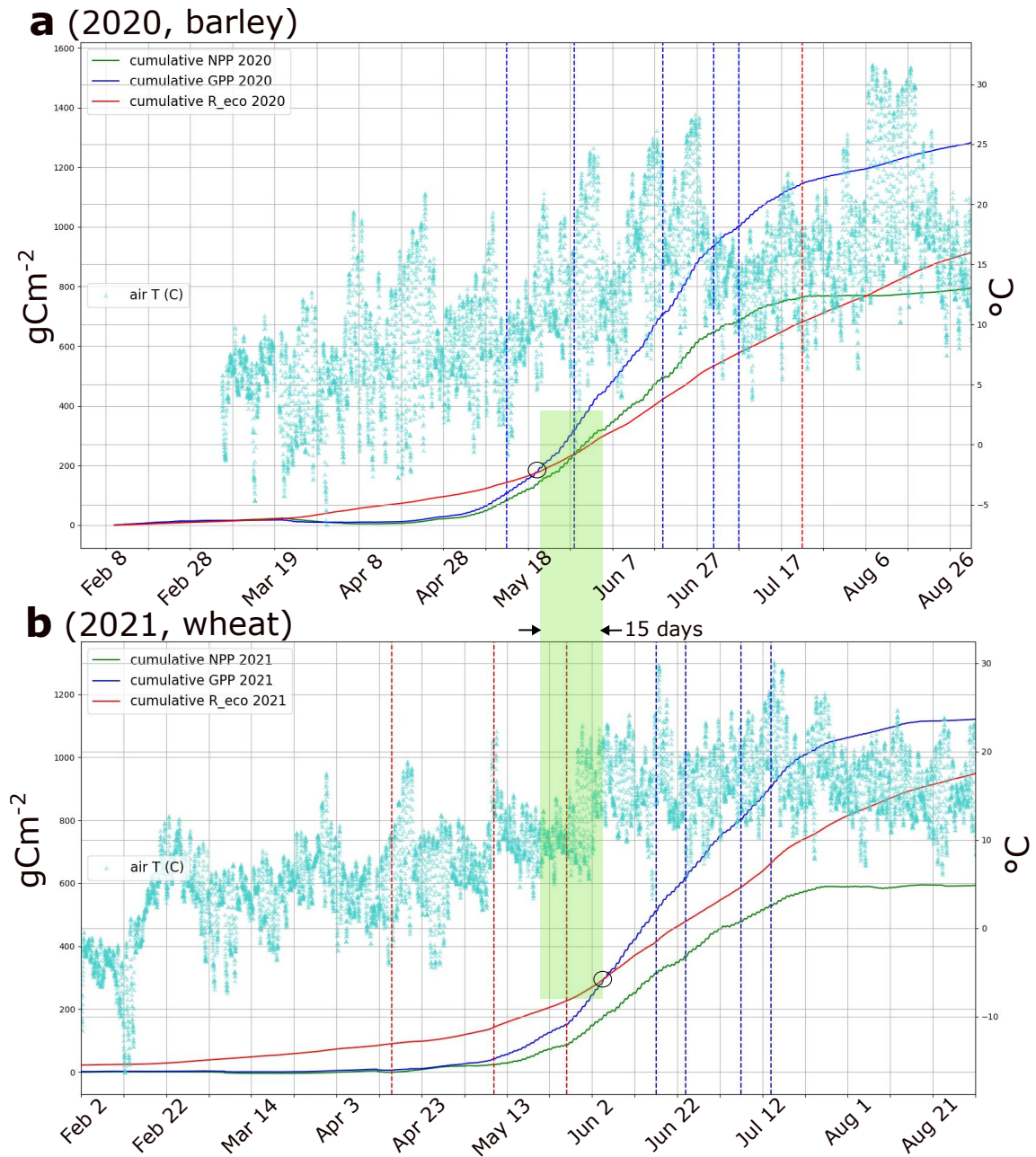


**Figure 12.** Estimated cumulative fluxes along the growing season of 2020 (a), and 2021 (b). GPP: gross primary productivity;  $R_{eco}$ : ecosystem respiration; NPP: net primary productivity. The red vertical lines indicate aboveground biomass (AGB) sampling dates, while the blue lines indicate dates in which both AGB sampling and UAV-LiDAR surveys took place. In both years, the black circles indicate the dates when GPP offsets  $R_{eco}$ . It can be observed how in 2021 this occurs on the 5<sup>th</sup> June, while in 2020 GPP reaches ecosystem respiratory losses on the 19<sup>th</sup> May, i.e. 16 days earlier. This delay in GPP during 2021 is partly explained due to the cold spell of February, damaging the early seedlings. The lack of temperatures at the beginning of 2020 (a) is due to a failure in the instrumental setup.

581 **References**

- 582 [1] David Laborde et al. “Agricultural subsidies and global greenhouse gas emissions”. In:  
583 *Nature communications* 12.1 (2021), p. 2601.
- 584 [2] John R Porter, Mark Howden, and Pete Smith. “Considering agriculture in IPCC assess-  
585 ments”. In: *Nature Climate Change* 7.10 (2017), pp. 680–683.
- 586 [3] Philip Thornton et al. “Agriculture in a changing climate: Keeping our cool in the face of  
587 the hothouse”. In: *Outlook on Agriculture* 47.4 (2018), pp. 283–290.
- 588 [4] P. R. Shukla et al. *Summary for policymakers, in Climate Change Land: An IPCC Special  
589 Report on Climate Change Desertification, Land Degradation, Sustainable Land Manage-  
590 ment, Food Security, Greenhouse Gas Fluxes in Terrestrial Ecosystems*. Tech. rep. Inter-  
591 governmental Panel on Climate Change, 2023.
- 592 [5] Marco Springmann et al. “Options for keeping the food system within environmental limits”.  
593 In: *Nature* 562.7728 (2018), pp. 519–525.
- 594 [6] Gerald C Nelson et al. “Climate change effects on agriculture: Economic responses to  
595 biophysical shocks”. In: *Proceedings of the National Academy of Sciences* 111.9 (2014),  
596 pp. 3274–3279.
- 597 [7] Mitchell C Hunter et al. “Agriculture in 2050: recalibrating targets for sustainable intensi-  
598 fication”. In: *Bioscience* 67.4 (2017), pp. 386–391.
- 599 [8] Hamid El Bilali et al. “Food and nutrition security and sustainability transitions in food  
600 systems”. In: *Food and energy security* 8.2 (2019), e00154.
- 601 [9] Jonathan A Foley et al. “Solutions for a cultivated planet”. In: *Nature* 478.7369 (2011),  
602 pp. 337–342.
- 603 [10] Tara Garnett et al. “Sustainable intensification in agriculture: premises and policies”. In:  
604 *Science* 341.6141 (2013), pp. 33–34.
- 605 [11] David J Mulla. “Twenty five years of remote sensing in precision agriculture: Key advances  
606 and remaining knowledge gaps”. In: *Biosystems engineering* 114.4 (2013), pp. 358–371.
- 607 [12] F Stuart Chapin, PA Matson, and PM Vitousek. *Principles of terrestrial ecosystem ecology*.  
608 *Principles of Terrestrial Ecosystem Ecology*. 2012.
- 609 [13] YM Zhang et al. “Vegetation carbon sequestration in the Loess Plateau under the syner-  
610 gistic effects of land cover change and elevations”. In: *Acta Ecologica Sinica* 42.10 (2022),  
611 pp. 3897–3908.
- 612 [14] Peter M Anthoni et al. “Winter wheat carbon exchange in Thuringia, Germany”. In: *Agric-  
613 cultural and Forest Meteorology* 121.1-2 (2004), pp. 55–67.
- 614 [15] Ulises Mariano Marconato, Roberto J Fernández, and Gabriela Posse Beaulieu. *Cropland  
615 Net Ecosystem Exchange Estimation for the Inland Pampas (Argentina) Using EVI, Land  
616 Cover Maps, and Eddy Covariance Fluxes*. Tech. rep. Frontiers Media, 2022.
- 617 [16] Arne Poyda et al. “Carbon fluxes and budgets of intensive crop rotations in two regional  
618 climates of southwest Germany”. In: *Agriculture, Ecosystems & Environment* 276 (2019),  
619 pp. 31–46.
- 620 [17] Anne-Katrin Prescher, Thomas Grünwald, and Christian Bernhofer. “Land use regulates  
621 carbon budgets in eastern Germany: From NEE to NBP”. In: *Agricultural and Forest Me-  
622 teorology* 150.7-8 (2010), pp. 1016–1025.

- 623 [18] Rasmus Jensen, Mathias Herbst, and Thomas Friborg. *Direct and indirect controls of the*  
624 *interannual variability in atmospheric CO<sub>2</sub> exchange of three contrasting ecosystems in*  
625 *Denmark*. 2016.
- 626 [19] Praveena Krishnan et al. “Factors controlling the interannual variability in the carbon  
627 balance of a southern boreal black spruce forest”. In: *Journal of Geophysical Research:*  
628 *Atmospheres* 113.D9 (2008).
- 629 [20] Christopher B Field and Jörg Kaduk. “The carbon balance of an old-growth forest: building  
630 across approaches”. In: *Ecosystems* 7 (2004), pp. 525–533.
- 631 [21] Mark E Harmon et al. “Production, respiration, and overall carbon balance in an old-growth  
632 Pseudotsuga-Tsuga forest ecosystem”. In: *Ecosystems* 7 (2004), pp. 498–512.
- 633 [22] Heather Keith, Brendan G Mackey, and David B Lindenmayer. “Re-evaluation of forest  
634 biomass carbon stocks and lessons from the world’s most carbon-dense forests”. In: *Pro-*  
635 *ceedings of the National Academy of Sciences* 106.28 (2009), pp. 11635–11640.
- 636 [23] Scott D Miller et al. “Biometric and micrometeorological measurements of tropical forest  
637 carbon balance”. In: *Ecological Applications* 14.sp4 (2004), pp. 114–126.
- 638 [24] Jian Wu et al. “Synthesis on the carbon budget and cycling in a Danish, temperate deciduous  
639 forest”. In: *Agricultural and Forest Meteorology* 181 (2013), pp. 94–107.
- 640 [25] Thomas Foken, Marc Aubinet, and Ray Leuning. “The eddy covariance method”. In: *Eddy*  
641 *covariance: a practical guide to measurement and data analysis*. Springer, 2011, pp. 1–19.
- 642 [26] Sheng Wang et al. “Temporal interpolation of land surface fluxes derived from remote  
643 sensing—results with an unmanned aerial system”. In: *Hydrology and Earth System Sciences*  
644 24.7 (2020), pp. 3643–3661.
- 645 [27] Helene Hoffmann et al. “Crop water stress maps for an entire growing season from visible  
646 and thermal UAV imagery”. In: *Biogeosciences* 13.24 (2016), pp. 6545–6563.
- 647 [28] Derek Hollenbeck and YangQuan Chen. “Multi-UAV method for continuous source rate  
648 estimation of fugitive gas emissions from a point source”. In: *2021 International Conference*  
649 *on Unmanned Aircraft Systems (ICUAS)*. IEEE. 2021, pp. 1308–1313.
- 650 [29] Derek Hollenbeck et al. “Evaluating a UAV-based mobile sensing system designed to quan-  
651 tify ecosystem-based methane”. In: *Authorea Preprints* (2022).
- 652 [30] Jaime C Revenga et al. “Above-Ground Biomass Prediction for Croplands at a Sub-Meter  
653 Resolution Using UAV–LiDAR and Machine Learning Methods”. In: *Remote Sensing* 14.16  
654 (2022), p. 3912.
- 655 [31] N Ace Pugh et al. “Temporal estimates of crop growth in sorghum and maize breeding  
656 enabled by unmanned aerial systems”. In: *The Plant Phenome Journal* 1.1 (2018), pp. 1–  
657 10.
- 658 [32] Wang Li et al. “Remote estimation of canopy height and aboveground biomass of maize  
659 using high-resolution stereo images from a low-cost unmanned aerial vehicle system”. In:  
660 *Ecological indicators* 67 (2016), pp. 637–648.
- 661 [33] Abdullah M Al-Sadi et al. “Genetic analysis reveals diversity and genetic relationship among  
662 Trichoderma isolates from potting media, cultivated soil and uncultivated soil”. In: *BMC*  
663 *microbiology* 15 (2015), pp. 1–11.
- 664 [34] Sebastian Varela et al. “Spatio-temporal evaluation of plant height in corn via unmanned  
665 aerial systems”. In: *Journal of Applied Remote Sensing* 11.3 (2017), pp. 036013–036013.

- 666 [35] J Bendig et al. “Very high resolution crop surface models (CSMs) from UAV-based stereo  
667 images for rice growth monitoring in Northeast China”. In: *Int. Arch. Photogramm. Remote*  
668 *Sens. Spat. Inf. Sci* 40 (2013), pp. 45–50.
- 669 [36] Juliane Bendig et al. “Estimating biomass of barley using crop surface models (CSMs)  
670 derived from UAV-based RGB imaging”. In: *Remote sensing* 6.11 (2014), pp. 10395–10412.
- 671 [37] Sebastian Brocks and Georg Bareth. “Estimating barley biomass with crop surface models  
672 from oblique RGB imagery”. In: *Remote Sensing* 10.2 (2018), p. 268.
- 673 [38] Tianxing Chu et al. “Cotton growth modeling and assessment using unmanned aircraft sys-  
674 tem visual-band imagery”. In: *Journal of Applied Remote Sensing* 10.3 (2016), pp. 036018–  
675 036018.
- 676 [39] T Jensen et al. “Detecting the attributes of a wheat crop using digital imagery acquired  
677 from a low-altitude platform”. In: *Computers and electronics in agriculture* 59.1-2 (2007),  
678 pp. 66–77.
- 679 [40] E Raymond Hunt et al. “NIR-green-blue high-resolution digital images for assessment of  
680 winter cover crop biomass”. In: *GIScience & remote sensing* 48.1 (2011), pp. 86–98.
- 681 [41] Maria Tattaris, Matthew P Reynolds, and Scott C Chapman. “A direct comparison of re-  
682 mote sensing approaches for high-throughput phenotyping in plant breeding”. In: *Frontiers*  
683 *in plant science* 7 (2016), p. 1131.
- 684 [42] Jakob Geipel et al. “A programmable aerial multispectral camera system for in-season crop  
685 biomass and nitrogen content estimation”. In: *Agriculture* 6.1 (2016), p. 4.
- 686 [43] Jibo Yue et al. “Estimation of winter wheat above-ground biomass using unmanned aerial  
687 vehicle-based snapshot hyperspectral sensor and crop height improved models”. In: *Remote*  
688 *Sensing* 9.7 (2017), p. 708.
- 689 [44] Roope Näsi et al. “Estimating biomass and nitrogen amount of barley and grass using UAV  
690 and aircraft based spectral and photogrammetric 3D features”. In: *Remote Sensing* 10.7  
691 (2018), p. 1082.
- 692 [45] Angela Kross et al. “Assessment of RapidEye vegetation indices for estimation of leaf area  
693 index and biomass in corn and soybean crops”. In: *International Journal of Applied Earth*  
694 *Observation and Geoinformation* 34 (2015), pp. 235–248.
- 695 [46] Kishore C Swain, Steven J Thomson, and Hemantha PW Jayasuriya. “Adoption of an  
696 unmanned helicopter for low-altitude remote sensing to estimate yield and total biomass of  
697 a rice crop”. In: *Transactions of the ASABE* 53.1 (2010), pp. 21–27.
- 698 [47] Jordan Steven Bates et al. “Estimating canopy density parameters time-series for winter  
699 wheat using UAS Mounted LiDAR”. In: *Remote Sensing* 13.4 (2021), p. 710.
- 700 [48] ICOS. *Integrated Carbon Observation System*. 2023. URL: <https://www.icos-cp.eu/>  
701 (visited on 02/04/2023).
- 702 [49] Danish Ministry of Environment. *Order on the use of fertilisers by agriculture for the*  
703 *2020/2021 planning period*. 2021. URL: [https://www.retsinformation.dk/eli/lta/](https://www.retsinformation.dk/eli/lta/2020/1166)  
704 [2020/1166](https://www.retsinformation.dk/eli/lta/2020/1166). (accessed: 25.10.2021).
- 705 [50] L Davidson et al. “Airborne to UAS LiDAR: An analysis of UAS LiDAR ground control  
706 targets”. In: *ISPRS Geospatial Week 2019* (2019).
- 707 [51] Bert Gielen et al. “Ancillary vegetation measurements at ICOS ecosystem stations”. In:  
708 *International Agrophysics* 32.4 (2018), pp. 645–664.

- 709 [52] Johanna Pausch and Yakov Kuzyakov. “Carbon input by roots into the soil: quantification  
710 of rhizodeposition from root to ecosystem scale”. In: *Global change biology* 24.1 (2018),  
711 pp. 1–12.
- 712 [53] J Swinnen, JA Van Veen, and RJSB Merckx. “<sup>14</sup>C pulse-labelling of field-grown spring  
713 wheat: an evaluation of its use in rhizosphere carbon budget estimations”. In: *Soil Biology  
714 and Biochemistry* 26.2 (1994), pp. 161–170.
- 715 [54] Erick Zagal, Sigfus Bjarnason, and ULF Olsson. “Carbon and nitrogen in the root-zone of  
716 barley (*Hordeum vulgare* L.) supplied with nitrogen fertilizer at two rates”. In: *Plant and  
717 Soil* 157 (1993), pp. 51–63.
- 718 [55] PJ Gregory and BJ Atwell. “The fate of carbon in pulse-labelled crops of barley and wheat”.  
719 In: *Plant and Soil* 136 (1991), pp. 205–213.
- 720 [56] Jan C Zadoks, Ting T Chang, Cal F Konzak, et al. “A decimal code for the growth stages  
721 of cereals.” In: *Weed research* 14.6 (1974), pp. 415–421.
- 722 [57] Dean Vickers and L Mahrt. “Quality control and flux sampling problems for tower and  
723 aircraft data”. In: *Journal of atmospheric and oceanic technology* 14.3 (1997), pp. 512–526.
- 724 [58] E. K. Webb, G. I. Pearman, and R. Leuning. “Correction of flux measurements for den-  
725 sity effects due to heat and water vapour transfer”. In: *Quarterly Journal of the Royal  
726 Meteorological Society* 106.447 (1980), pp. 85–100.
- 727 [59] Claudia Liebenthal and Thomas Foken. “On the significance of the Webb correction to  
728 fluxes”. In: *Boundary-Layer Meteorology* 109 (2003), pp. 99–106.
- 729 [60] JB Moncrieff et al. “A system to measure surface fluxes of momentum, sensible heat, water  
730 vapour and carbon dioxide”. In: *Journal of Hydrology* 188 (1997), pp. 589–611.
- 731 [61] S Sabbatini and D Papale. *ICOS Ecosystem Instructions for Turbulent Flux Measurements  
732 of CO<sub>2</sub>, Energy and Momentum (Version 20180110)*, ICOS Ecosystem Thematic Centre.  
733 2017.
- 734 [62] Dario Papale et al. “Towards a standardized processing of Net Ecosystem Exchange mea-  
735 sured with eddy covariance technique: algorithms and uncertainty estimation”. In: *Biogeos-  
736 sciences* 3.4 (2006), pp. 571–583.
- 737 [63] Markus Reichstein et al. “On the separation of net ecosystem exchange into assimilation  
738 and ecosystem respiration: review and improved algorithm”. In: *Global change biology* 11.9  
739 (2005), pp. 1424–1439.
- 740 [64] Natascha Kljun, MW Rotach, and HP Schmid. “A three-dimensional backward Lagrangian  
741 footprint model for a wide range of boundary-layer stratifications”. In: *Boundary-Layer  
742 Meteorology* 103 (2002), pp. 205–226.
- 743 [65] John Lloyd and JA Taylor. “On the temperature dependence of soil respiration”. In: *Func-  
744 tional ecology* (1994), pp. 315–323.
- 745 [66] Peter J Huber. “Robust statistics”. In: *International encyclopedia of statistical science*.  
746 Springer, 2011, pp. 1248–1251.
- 747 [67] Art B Owen. “A robust hybrid of lasso and ridge regression”. In: *Contemporary Mathematics*  
748 443.7 (2007), pp. 59–72.
- 749 [68] Pierre Geurts, Damien Ernst, and Louis Wehenkel. “Extremely randomized trees”. In: *Ma-  
750 chine learning* 63.1 (2006), pp. 3–42.
- 751 [69] Tianqi Chen et al. “Xgboost: extreme gradient boosting”. In: *R package version 0.4-2* 1.4  
752 (2015), pp. 1–4.
- 753 [70] Leo Breiman. “Random forests”. In: *Machine learning* 45.1 (2001), pp. 5–32.

- 754 [71] Teng Hu et al. “Root biomass in cereals, catch crops and weeds can be reliably estimated  
755 without considering aboveground biomass”. In: *Agriculture, Ecosystems & Environment* 251  
756 (2018), pp. 141–148.
- 757 [72] Yakov Kuzyakov and Grzegorz Domanski. “Carbon input by plants into the soil. Review”.  
758 In: *Journal of Plant Nutrition and Soil Science* 163.4 (2000), pp. 421–431.
- 759 [73] JA Palta and PJ Gregory. “Drought affects the fluxes of carbon to roots and soil in <sup>13</sup>C  
760 pulse-labelled plants of wheat”. In: *Soil Biology and Biochemistry* 29.9-10 (1997), pp. 1395–  
761 1403.
- 762 [74] Ernest C Large et al. “Growth stages in cereals. Illustration of the Feekes scale.” In: *Plant*  
763 *pathology* 3 (1954), pp. 128–129.
- 764 [75] Ngonidzashe Chirinda, Jørgen E Olesen, and John R Porter. “Root carbon input in organic  
765 and inorganic fertilizer-based systems”. In: *Plant and Soil* 359 (2012), pp. 321–333.
- 766 [76] Shai Ben-David et al. “A theory of learning from different domains”. In: *Machine learning*  
767 79 (2010), pp. 151–175.
- 768 [77] Joaquin Quinonero-Candela et al. *Dataset shift in machine learning*. Mit Press, 2008.
- 769 [78] Afshin Soltani. *Modeling physiology of crop development, growth and yield*. CABi, 2012.